pollutants

MDPI

Article

Selective Oxidation Desulfurization of Kerosene Using Transition Metal-Loaded Natural Clinoptilolite

Dhuha Jawad Hussein [1,2], Hind Shabbani [2,*], Mohammed Ali Mutar [3], C. T. Tye [1] and M. R. Othman [1,*]

[1] School of Chemical Engineering, Universiti Sains Malaysia, Nibong Tebal 14300, Malaysia
[2] Chemical Engineering Department, College of Engineering, University of AL-Qadisiyah, Engineering Campus, AL-Diwaniyah 58001, Iraq
[3] Department of Chemistry, College of Sciences, University of Al-Qadisiyah, AL Diwaniyah 58001, Iraq
* Correspondence: hind.shabbani@qu.edu.iq (H.S.); chroslee@usm.my (M.R.O.)

Abstract

Effective desulfurization techniques are vital, as the presence of sulfur compounds in kerosene presents serious operational and environmental problems. This study used formic acid and hydrogen peroxide in a selective oxidation method to examine the effectiveness of treated natural clinoptilolite as an adsorbent for eliminating sulfur compounds from kerosene. Natural clinoptilolite was heated to 500 °C and rinsed with nitric acid. This sample was subsequently loaded with four metals (Mg, Cu, Co, and Fe) at 0.2 M concentrations at 70 °C for five hours each. To detect structural and chemical changes caused by treatment and metal loading, the prepared samples were characterized with SEM, EDS, XRD, FTIR, and BET. NZCAN had the highest BET at 26.32 m^2/g, followed by cobalt-loaded clinoptilolite at 24.16 m^2/g. Desulfurization was carried out on a kerosene sample having an initial sulfur level of 3100 ppm. The NZCAN sample had the highest desulfurization effectiveness (84.13%), followed by the cobalt-loaded zeolite sample (83.4%), making it the best of the mineral-loaded samples. These findings suggest that thermal and acid treatment of natural clinoptilolite is sufficient for achieving good desulfurization efficiency. Additionally, the cobalt-loaded clinoptilolite retained a similar efficiency; however, this study did not show a catalytic role for cobalt, which calls for future research.

Keywords: oxidative-adsorptive desulfurization (OADS); natural zeolite-clinoptilolite; kerosene; transition-metal loading; nitric acid treatment

1. Introduction

Since sulfur compounds in petroleum fractions like kerosene cause SO_x emissions, equipment corrosion, and catalyst poisoning, stricter restrictions now require ultra-low sulfur fuels [1]. Because of steric hindrance, conventional hydrodesulfurization (HDS) struggles with refractory chemicals like dibenzothiophene (DBT) and necessitates high temperatures, high hydrogen pressure, and costly catalysts [2,3]. An option is oxidative desulfurization (ODS), in which sulfur compounds are converted into polar sulfoxides and sulfones under mild circumstances without hydrogen by oxidants such as H_2O_2. These products are subsequently extracted or adsorbed [4–6]. Because the sulfones are caught on a polar solid as they form, oxidative-adsorptive desulfurization (OADS) completes both processes in the same solution, simplifying the process and improving selectivity toward sulfur compounds over sulfur-free aromatics [7–9]. Because they combine adsorptive, molecular-sieving, and acidic capabilities at a cheaper cost than synthetic zeolites, natural zeolites are appealing adsorbents for this purpose [10,11].

Check for updates

Academic Editor: Paolo Pastorino

Received: 23 August 2026
Revised: 5 November 2026
Accepted: 9 November 2026
Published: 23 November 2026

Copyright: © 2026 by the authors. Licensee MDPI, Basel, Switzerland. This article is an open access article distributed under the terms and conditions of the Creative Commons Attribution (CC BY) license.

The most prevalent naturally occurring zeolite, clinoptilolite, is a crystalline aluminosilicate with a three-dimensional network of channels connecting SiO_4 and AlO_4 tetrahedra. It has a silica-rich content (Si/Al = 2 to 5) depending on the geological source and a monoclinic structure [11–13]. Its ion-exchange capacity, adsorption ability, and strong thermal stability are its defining characteristics. It occurs naturally over extended geological periods through volcanic and marine processes [10,14]. These characteristics, along with their affordability, accessibility, and environmental friendliness, makes clinoptilolite a good support for transition-metal catalysts because of its pore structure and ion-exchange capacity, which enable metal loading and dispersion [15]. However, large compounds like DBT and benzothiophene (BT) cannot diffuse through the channels due to its low acidity and small micropores [16].

HNO_3 treatment is a popular strategy to get around these restrictions. It eliminates impurities and framework aluminum, boosts the Si/Al ratio, expands surface area, creates mesopores that enhance diffusion, and changes the acidity from Brønsted to Lewis sites. On the other hand, the crystalline structure may collapse with severe treatment [4,16]. Aromatics and sulfur compounds vie for the same locations on the modified zeolite since adsorption is still primarily physical [14]. More selective locations may be introduced by loading metals. Cu, Co, and Fe cations can bind the sulfur atom as Lewis acids, Cu and Co can interact with the thiophene ring by π-complexation, and Fe, Co, and Cu can activate H_2O_2 through Fenton-like reactions [17,18]. However, the metal, loading technique, support, and operating circumstances all affect the benefit, and excessive H_2O_2 breakdown can reduce oxidant efficiency [19]. For oxidation processes, clinoptilolite has been loaded with Fe, Cu, and Co [20]. For sulfur adsorption, it has been loaded with Ag^+, Hg^{2+}, Ni^{2+}, and Ce^{3+} [20–24], including an acid-treated, calcined sample loaded with Ni^{2+}, Cu^{2+}, and Ce^{3+} [23–25]. It has also been found that the removal of thiophene, BT, and DBT is significantly improved by dealuminating Ni-exchanged clinoptilolite [26]. However, the majority of this research relied on some of the most effective metals (Ag, Hg), which are costly or hazardous, employed model solutions and adsorption alone, and applied various metals, supports, and conditions [27]. Rarely were control samples devoid of transition metals used, and the relationship between material characteristics and actual fuel performance has rarely been investigated. To the best of our knowledge, OADS of actual kerosene has not been compared under equivalent conditions between Co, Cu, Fe, and Mg-loaded HNO_3-treated clinoptilolite [20].

The novelty of this work lies in the direct comparison of raw, acid-activated and Fe-, Cu-, Co- and Mg-loaded natural clinoptilolite under identical conditions, using real refinery kerosene (3100 ppm S) and an H_2O_2/HCOOH oxidation system, rather than model fuels. Cu, Co, Fe, and Mg were selected because they are readily available, reasonably priced, and have distinct functions in sulfur binding and oxidant activation. Mg^{2+}, which lacks d electrons, is used as a control to distinguish between basic surface alteration and transition-metal effects. All metal-loaded samples were examined under the identical conditions after the calcination temperature, reaction temperature, reaction time, and HCOOH/H_2O_2 ratio were first optimized on the acid-treated sample alone. The objectives are to compare the impact of each metal and its loading on sulfur and aromatic removal in relation to the acid-treated support, to connect textural, structural, and thermal features to desulfurization performance, and to differentiate transition-metal effects from straightforward surface alteration.

2. Materials and Methods

Al-Shanafiyah refinery provided kerosene feedstock, which had an initial sulfur level of 3100 ppm (ASTM D4294) [28]. The physicochemical characteristics of this raw kerosene are detailed in Table 1. Natural volcanic zeolite (clinoptilolite type) was obtained from a

local supplier and subsequently purified and characterized to confirm its surface properties. All chemical reagents were of analytical reagent (AR) grade and used without further purification. Nitric acid (HNO_3, 69–71% AR) was procured from SD Fine-Chem Limited (SDFCL), Mumbai, India. Formic acid (HCOOH, 85%) and hydrogen peroxide (H_2O_2, 35%) were supplied by SIGMA-ALDRICH, Steinheim, Germany, and PanReac AppliChem, Darmstadt, Germany, respectively. Transition metal salts, including cobalt(II) chloride ($CoCl_2$, 99% AR) and copper(II) chloride ($CuCl_2$, 99% AR), were obtained from SIG-MA-ALDRICH, Germany. Iron(III) chloride ($FeCl_3$, 99% AR) and magnesium(II) chloride ($MgCl_2$, 99% AR) were sourced from Pallav, India. Dimethylformamide (DMF, 99.5%) was purchased from HIMEDIA. Distilled water (99% purity) and deionized water were provided by Al-Buruj in Al-Diwaniyah, Iraq.

Table 1. Physical properties of kerosene taken from Al-Shanafiyah refinery.

Property	Value
Density 15 °C	0.7875 g/cm^3
Flash point	48 °C
Color (Saybolt)	+30
Sulfur Content	3100 ppm
Doctor test	Positive
Smoke point	26.3 mm
Free water	Nil

2.1. Preparation of Zeolite Catalyst

Natural clinoptilolite was crushed and washed. The ground natural clinoptilolite is denoted as NZ. The NZ sample was then sieved to obtain 300 µm utilizing an electro-vibrating sieve. The sieved material was then dried overnight at 40 °C. Approximately 50 gm of the dried material was calcined in a furnace for 4 h at 500 °C. The calcined sample was then allowed to cool down to room temperature prior to utilization in sulfur removal and denoted as NZC. Preliminary investigations showed that heat treatment at 500 °C with particles sized according to the 300 µm standard produced the lowest residual sulfur concentration; as a result, these parameters were used for further experiments.

The NZC sample was subsequently activated by immersing it in 2 M nitric acid (HNO_3) under vigorous stirring and heating to 83 °C for 2 h to ensure complete dealumination and surface modification. After cooling to room temperature, the solid was collected by filtration and washing repeatedly with water until the pH reached 7 to ensure complete removal of the HNO_3. The resulting sample was heated to 100 °C over-night to ensure complete removal of moisture prior to use. Hereafter, the sample is denoted as NZCAN.

Metal loading of zeolite was achieved by utilizing the NZCAN as the supporting material. Four different metal loadings (Fe, Cu, Mg, and Co) were prepared from their salts ($FeCl_3$, $CuCl_2$, $MgCl_2$, and $CoCl_2$). To prepare the metal-loaded zeolite, the NZCAN sample was used as the supporting material by dissolving it in 100 mL of deionized water to prepare a 0.2 M solution with metal salts. The solution was subsequently transferred into a 250 mL beaker, and 3 g of zeolite was added and stirred for 5 h at 70 °C. The solid sample was then recovered by vacuum filtration and washed repeatedly with deionized water and then heated at 90 °C overnight to ensure moisture removal. Identical steps were used to prepare all metal-loaded samples (0.2 M salt solution, 3 g NZCAN, 70 °C, 5 h). Therefore, rather than using the same metal content, the comparison is based on the same preparation circumstances.

Summarized steps of catalyst preparation are illustrated in Figure 1.

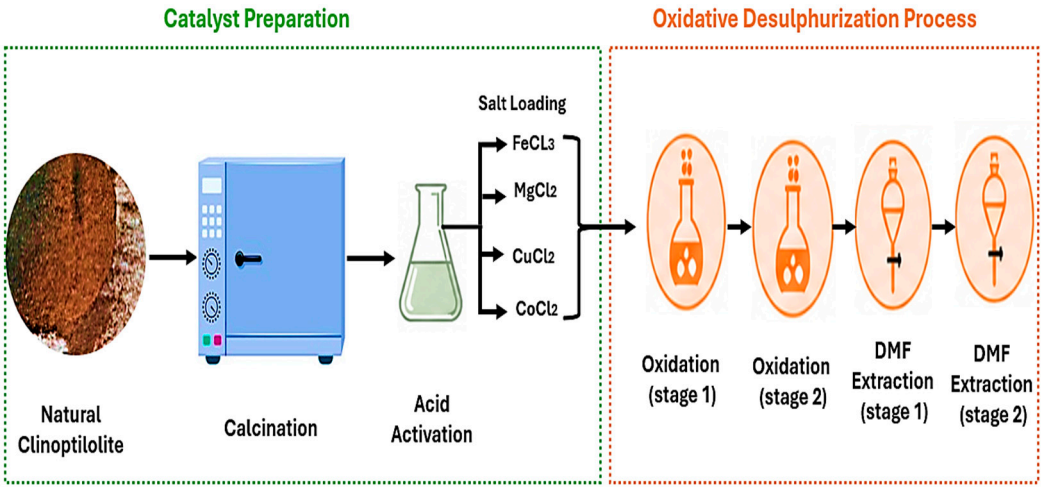

Figure 1. Experimental workflow for catalyst preparation, and the oxidative desulfurization process.

After the oxidation process, the spent sample was collected and regenerated by washing with deionized water and filtering it in a filter funnel. The sample was then collected and dried in an oven for 4 h and then placed in a furnace at 400 °C for 2 h under N_2 flow. All the samples were tested under the same kerosene feedstock with the same initial concentration of sulfur, same oxidant composition and amount, same temperature and reaction time, identical stirring speed and solid dosage, and the same DMF extraction procedure to allow direct comparison. The comparison between the metals is based on the identical conditions rather than an equal metal content.

Spent NZCAN was revived for 120 min at 400 °C in a muffle furnace, and it was then reused under the same oxidation adsorption conditions as the fresh samples (35 °C, 140 min). Furthermore, 30 g of recovered material made up the regeneration batch.

2.2. Catalytic Oxidative Desulfurization and Extractions of Kerosene

Catalytic oxidative desulfurization (ODS) of kerosene was conducted in a 250 mL three-neck flask mounted on a temperature-controlled oil bath, fitted with a condenser and magnetic stirrer. In a batch experiment, 100 mL of kerosene sample was placed in the reactor. Furthermore, 25 mL of H_2O_2 and 30 mL of HCOOH were added as oxidizers followed by the addition of 2.0 g of the mineral-loaded zeolite catalyst. The reaction was carried out at 35 °C and stirred for 140 min with constant air bubbling. A schematic diagram of the experimental setup is shown in Figure 1.

The reaction conditions were established at 35 °C for 140 min with a fixed molar ratio of 2.42:1 for the oxidation system HCOOH:H_2O_2 and mixing speed of 750 rpm, based on preliminary experiments and optimization of the acid-activated zeolite support. By establishing a strong baseline for the desulfurization process using the unmodified support, these parameters made it possible to accurately and independently evaluate the catalytic role of the transition metals integrated into the support.

Kerosene extraction was carried out by mixing 80 mL of the sample with 80 mL of dimethylformamide (DMF) solvent in a glass flask using a magnetic stirrer. The mixture was then stirred at 50 °C for 30 min. Afterward, the mixture was placed in an extraction funnel to separate the kerosene from the solvent. Two layers formed: the lower layer, consisting of solvent and sulfur compounds, separated from the upper layer of pure kerosene due to the difference in density. This process was repeated twice as depicted in Figure 1.

The desulfurization procedure and catalyst quantities employed in the trials are summarized in Table 2. Each experiment was carried out three times using different batches, and

the results are shown in the table as the arithmetic mean of three replicates with standard deviation of sulfur removal not exceeding 0.032% for any sample.

Table 2. Experimental conditions and oxidative desulfurization performance of untreated, acid-activated, and metal salt-modified clinoptilolite catalysts.

Catalyst	Salt Concentration in Solution (M)	Regeneration (°C/min)	Reaction Time (min)	Reaction Temperature (°C)	Initial Sulfur Content (ppm)	Residual Sulfur Content (ppm)
NZ	-	-	140	35	3100	1332.7
NZCAN	-	-	140	35	3100	492
Fe/NZCAN	0.2	-	140	35	3100	739.7
Mg/NZCAN	0.2	-	140	35	3100	565
Cu/NZCAN	0.2	-	140	35	3100	663.1
Co/NZCAN	0.2	-	140	35	3100	514.2
Regenerated NZCAN	-	400/120	140	35	3100	499.1

The ODS method of desulfurization uses both oxidation and adsorption. First, performic acid (Equation (1)), a potent oxidant that converts non-polar dibenzothiophene (DBT) into highly polar DBT-sulfone (Equation (2)), is created when formic acid and H_2O_2 combine in situ [19]:

$$HCOOH + H_2O_2 \rightleftharpoons HCOOOH + H_2O \quad (1)$$

$$DBT \rightarrow DBT\text{-}Sulfoxide \rightarrow DBT\text{-}Sulfone \quad (2)$$

After that, the sulfone is firmly adsorbed onto the surface of the transformed clinoptilolite. By serving as Lewis-acid sites and activating peroxides through Fenton-like redox cycles (Equations (3) and (4)), the supporting metals (Fe, Cu, and Co) quicken this transition [29]:

$$M^{n+} + H_2O_2 \rightarrow M^{(n+1)+} + \bullet OH + OH^- \quad (3)$$

$$M^{(n+1)+} + H_2O_2 \rightarrow M^{n+} + HOO\bullet + H^+ \quad (4)$$

where M is the metal ion supported on the zeolite. Because formic acid scavenges OH radicals, the peracid route continues to be dominant even if metals can produce reactive oxygen species (ROS). This process is suggested based on previous literature; direct ROS detection was not carried out [29–31].

2.3. Catalyst Characterization

Sulfur content was measured using a Sindie 7039 sulfur analyzer (manufactured by XOS/PAC), which utilizes Monochromatic Wavelength Dispersive X-ray Fluorescence (MWDXRF) technology and complies with ASTM D7039 and ISO 20884 standards [28], including calibration with certified sulfur standards as specified in the standard. The method measures total sulfur only; individual sulfur species were not identified. The device operates using a standard electrical power supply and requires no carrier or combustion gases. Analysis was conducted at the Oil Research and Development Center of the Iraqi Ministry of Oil, Baghdad.

Surface morphological characterization was conducted using a VEGA\TESCAN (VEGA, TESCAN, Brno, Czech Republic) scanning electron microscope (SEM) at the Nanotechnology and Advanced Materials Research Centre at the University of Technology, Baghdad. To ensure a consistent comparative analysis between the six zeolite samples, all

micrographs were acquired at 5000×. A 10 μm scale bar was utilized to provide a precise reference for evaluating structural changes, such as surface roughness and pore development, resulting from the calcination and nitric acid treatments.

Phase identification and structural analysis of the modified zeolite samples (the natural clinoptilolite, the sample after calcination and treated with nitric acid, and then the samples loaded with the four metals: magnesium, iron, cobalt, and copper) were conducted via X-ray diffraction (XRD) using a Cu Kα radiation source (λ= 1.54060 Å) operating at 40 kV and 30 mA. The diffraction patterns were recorded over a 2 θ range of 10° to 80° with a scan step of 0.0400° and a continuous counting time of 0.24 s per step. These measurements were performed at the Nanotechnology and Advanced Materials Research Centre at the University of Technology, Baghdad.

Structural characterization of a zeolite catalyst was performed using Fourier transform infrared spectroscopy (FTIR). The analysis was conducted using a Bruker FTIR spectrometer (Bruker Corporation, Billerica, MA, USA) in the wavenumber range of 400–4000 cm^{-1}. Spectra were recorded in transmittance mode (%T) at room temperature, at the Nanotechnology and Advanced Materials Research Centre at the University of Technology, Baghdad.

The specific surface area and pore characteristics of the NZCAN, Co/NZCAN, Mg/NZCAN, Cu/NZCAN and Fe/NZCAN samples were determined via BET analysis using micromeritics ASAP 2020 volumetric analyzers (Micromeritics Instrument Corporation, Norcross, GA, USA). Prior to measurement, a 0.1200 g sample was degassed and dried at 150 °C for 6 h to remove any residual moisture and adsorbed species from the zeolite framework. This analysis was performed at the Oil Research and Development Center of the Iraqi Ministry of Oil in Baghdad.

3. Results and Discussions

The morphology of the NZ region is shown in Figure 2a, revealing a distinctive arrangement of planar and lamellar crystals. These crystalline sheets are characterized by their organization and large interparticle porosity, reflecting the fundamental structure of the clinoptilolite phase [7,32,33]. The heterogeneous particle distribution and wide variation in crystal dimensions are characteristic of unprocessed primary mineral materials, where the natural growth process results in a diverse and irregular structural orientation [34].

Figure 2b shows the NZCAN results, which show a dense, well-defined crystalline morphology with enhanced surface roughness [35]. This alteration primarily aims to remove framework exchangeable cations and selectively dealuminate the framework, which drastically changes the surface chemistry [4,33,36]. The resulting topography, which maintains the underlying crystalline structure of clinoptilolite, might provide a very active interface for sulfur oxidation [37]. Maintaining the high catalytic activity necessary for the oxidative process depends on this combination of increased surface area and structural stability [38].

In the morphology, it was observed that Mg/NZCAN has irregularly shaped crystals of varying sizes (5–20 microns) as shown in Figure 2c. The surface is rough and porous. Medium to high agglomeration was observed, with the particles clearly attached [18]. The mineral distribution is uneven, and there are light-colored deposits, indicating mineral deposition. Some areas are loaded with a higher density. The deposits appear to cover parts of the crystal surfaces, consistent with the large decrease in surface area [39].

Co/NZCAN (Figure 2d) shows a relatively smooth, continuous surface with few visible deposits, located mainly at the crystal edges, and an open cavity can be seen. No extensive surface coverage is observed, consistent with Co^{2+} species interacting with the zeolite framework mainly by ion exchange and with the small loss of surface area (8%) compared with NZCAN.

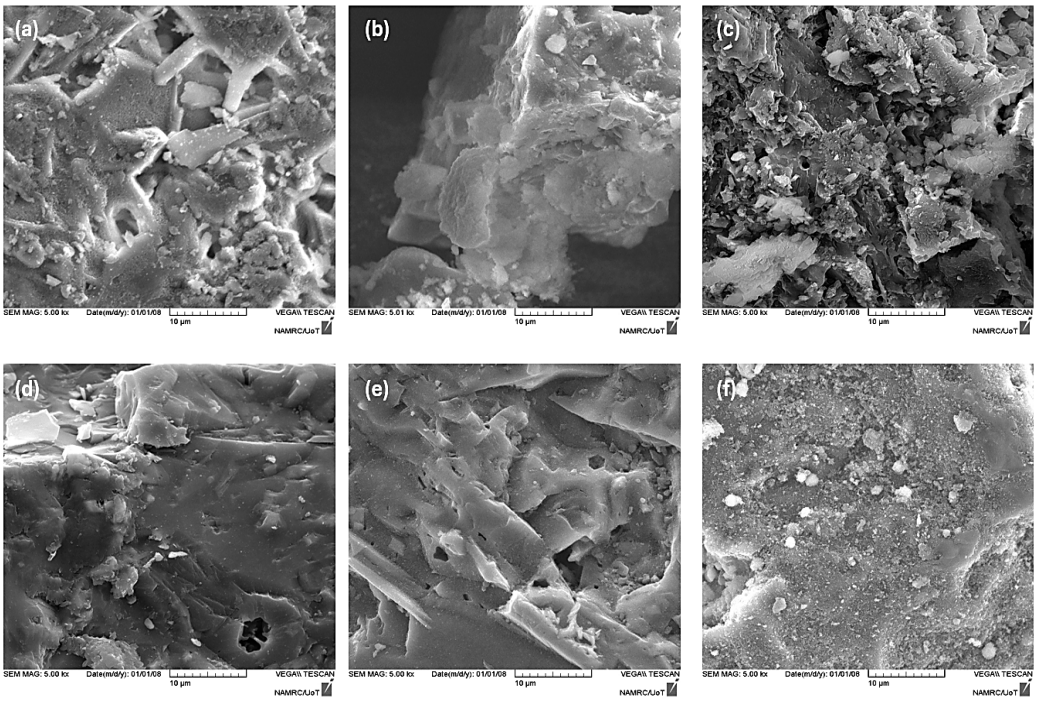

Figure 2. SEM images of (**a**) NZ, (**b**) NZCAN, (**c**) Mg/NZCAN, (**d**) Cu/NZCAN, (**e**) Co/NZCAN and (**f**) Fe/NZCAN.

The morphology of Cu/NZCAN is characterized by relatively large crystals with sharp edges, a platy and layered structure as shown in Figure 2e. The aggregates are large, compact masses with interparticle adhesion. The mineral distribution is moderately homogeneous, with some light-colored copper deposits present on the surface [20]. Porosity is moderate, and there are closed cavities due to the aggregates and the platy structure, which may restrict copper access to the pores [20,22].

The morphology of Fe/NZCAN is characterized by very small, homogeneous particles with a more uniform particle size distribution and a relatively smooth surface with fine, dispersed particles as shown in Figure 2f. Agglomeration is low, with well-dispersed, separate particles, exhibiting better distribution than other minerals [22]. The iron particles are evenly distributed, and the surface is uniformly covered with fine, sub-micrometer particles, most likely iron hydroxide/oxide deposits [20,40].

The Si/Al ratio did not change following calcination and acid activation (2.59 for NZ vs. 2.57 for NZCAN), according to EDS analysis (Figure 3), indicating that the framework was not considerably dealuminated. Both Si and Al appear to be higher in NZCAN (19.7 to 23.6% and 7.6 to 9.2%), but they increased by the same factor (about 1.2), which is not framework enrichment but rather a normalization effect from the loss of other components. Ca only slightly dropped (approximately 16%), but Na, Mg, and Fe declined by roughly 37%, 42%, and 32%, respectively, in relation to Si. K did not actually decline (the 21% increase is within the semi-quantitative EDS error). This is consistent with the known behavior of clinoptilolite in acid, where the framework stays intact while exchangeable cations and impurity phases are leached away [13]. The burning of organic materials and the loss of adsorbed water during calcination are most likely the causes of the decreased C (2.0 to 1.5%) and O (51.1 to 48.6%).

The same is indicated by FTIR. Both samples exhibit the Si–O–Si/Si–O–Al asymmetric stretching band (1050–1075 cm^{-1}), which is consistent with the unchanged Si/Al ratio. Its little shift (about 10 cm^{-1}) is more likely to reflect changes in hydration and extra-framework cations than dealumination. The reduced carbon content from EDS is consistent with the

weaker C–H bands in NZCAN at 1457 and roughly 2988 cm^{-1}. The loss of Na, Mg, and Fe is only substantiated by EDS because FTIR is unable to identify exchangeable cations.

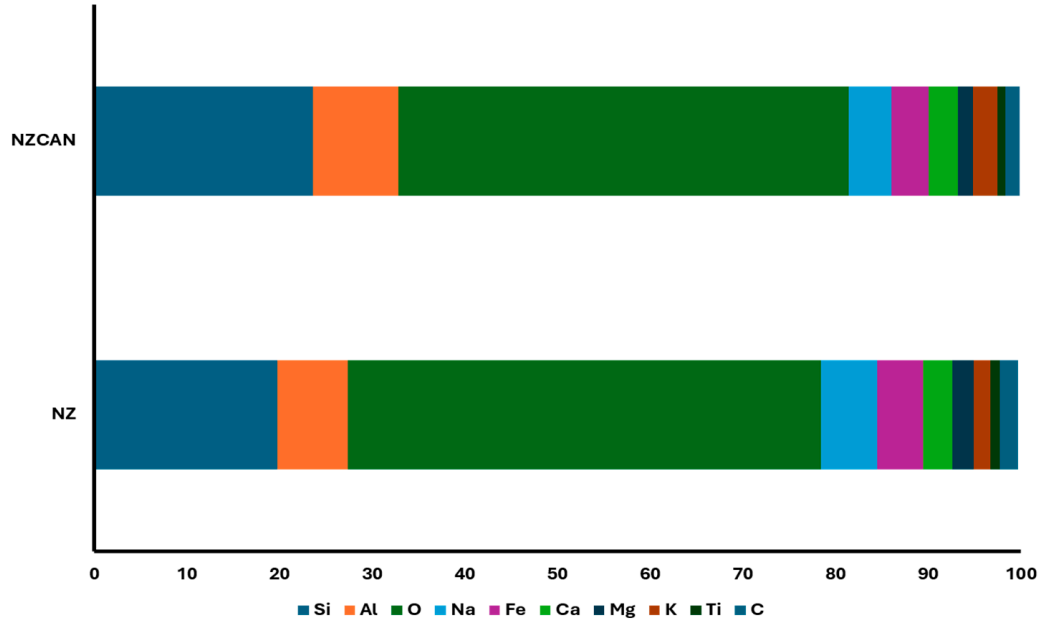

Figure 3. EDS analysis of NZ and NZCAN catalyst.

Residual sulfur decreased from 43% to 15.9%, while desulfurization efficiency rose from 57% for NZ to 84.13% for NZCAN (+27.1 percentage points). Dealumination cannot account for this gain because Si/Al remained unchanged. It is most likely associated with the elimination of iron-containing species, exchangeable cations (Na, Mg), adsorbed water, and organic residues, which likely expanded the pores and increased the number of adsorption sites available to sulfur compounds in kerosene [33,41].

The XRD plot of the natural clinoptilolite (NZ) shown in Figure 4 exhibited a crystalline pattern that differed in some details from that of the treated sample. The strongest reflectance peak was recorded at $2\theta = 30.85°$ with an interpolation distance d = 2.8958 Å, followed by a peak at 35.52° with a relative intensity of 80%, and then a peak at 30.22° with an intensity of 55% [33,37]. The overall intensity of the peaks was noticeably lower compared to the treated sample (highest absolute intensity ~56 Hz versus ~81 in the treated sample), reflecting the presence of mineral impurities and clay materials filling the pores and weakening the diffraction uniformity [42]. A distinct peak was also observed at 71.84° with a relative intensity of 55%, which was absent or weak in most of the other samples and may indicate the presence of an associated mineral phase such as feldspar or quartz in the raw material [37,43].

The calcination and nitric acid (NZCAN) washing processes resulted in significant changes in the XRD plot as shown in Figure 4. The strongest reflectance peak shifted from 30.85° in the raw sample to 29.98° with an interfacial distance d = 2.9784 Å, accompanied by a marked increase in the intensity of the main peaks (100% relative intensity versus 100% of the raw material, but with a higher absolute intensity); this means that by eliminating amorphous clay, contaminants, and obstructing ions, the acid treatment actually increased the sample's overall crystallinity and framework exposure rather than merely altering its internal peak ratios [4,39]. This improvement in crystal regularity is attributed to the removal of impurities and pore-clogging clay materials during the acid treatment, as well as the removal of exchangeable ions from their positions within the channels, thus highlighting

the zeolite framework peaks more clearly. A strong peak also appeared at 35.84° with an intensity of 95%, confirming the structural integrity of the clinoptilolite after treatment [4].

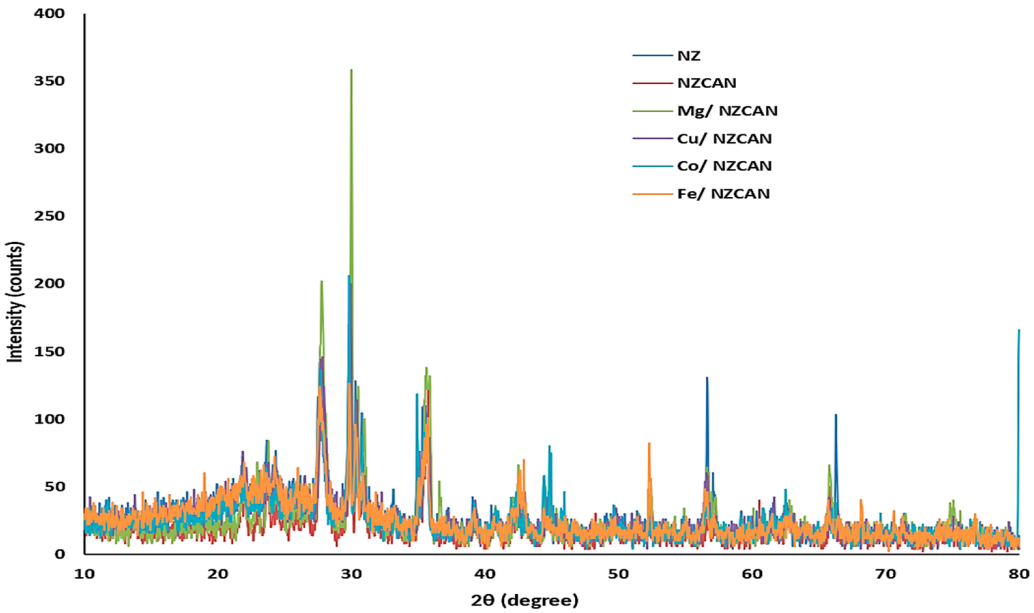

Figure 4. XRD of NZ, NZCAN, Mg/NZCAN, Cu/NZCAN, Co/NZCAN, and Fe/NZCAN.

A notable shift in the crystalline apex distribution was observed for Mg/NZCAN, with the strongest peak now at 2θ = 56.68° (d = 1.6211 Å) instead of the usual ~30°, while the peak at 29.86° retained its intensity at 93% as shown in Figure 4. Without causing the overall zeolite framework to disintegrate, this shift most likely represents a new spatial distribution of magnesium ions within the zeolite channels or the creation of surface compounds with a different crystalline structure [44,45].

For Cu/NZCAN with the strongest peak measured at 2θ = 29.96° (d = 2.9802 Å) and a noteworthy peak at 35.70°, this sample's XRD peak pattern closely matched that of the base sample. This suggests that copper ions were mainly kept in the zeolite channels' ion-exchange sites without affecting the material's structural identity [20,46].

According to the crystalline peak distribution for Co/NZCAN in Figure 4, this sample resembles the base sample the most. The main peaks retained their relative intensities and angular locations, suggesting that cobalt ions were dispersed over the zeolite surface without deeply penetrating the interior crystalline structure [21,47,48].

As seen in Figure 4, this specimen Fe/NZCAN was identified by the emergence of a new, noticeable reflectance peak at 2θ = 52.34° with a relative intensity of 84% [20,37]. It is not present in the raw material or any other specimen. This peak indicates that a crystalline phase of iron oxides, such as Fe_2O_3 (hematite) or Fe_3O_4 (magnetite), may have formed on the zeolite's surface or inside its porous structure. The absence of structural breakdown was confirmed by the principal clinoptilolite peaks maintaining their places [21,49].

The FTIR spectrum of raw clinoptilolite (NZ) exhibits several characteristic bands associated with the aluminosilicate framework (Figure 5). A strong, broad band appears in the 1049–1065 cm^{-1} range, attributed to the asymmetric stretching vibration of Si–O–Si/Si–O–Al bonds. The symmetric stretching vibration of these bonds is identified by two bands of medium-to-weak intensity at 669 and 705 cm^{-1} [20]. A medium-intensity band at 591 cm^{-1} is assigned to the double ring (D6R) [12] vibration within the aluminosilicate framework, which serves as an indicator of the zeolite's crystalline structure [38]. Furthermore, two weak-intensity bands are observed at 1457 and 2987 cm^{-1} [20]; these may be attributed to C–H stretching or bending vibrations, or potentially to the presence of trace carbonate

impurities. These findings support the aluminosilicate composition of the raw clinoptilolite and are consistent with previous research [50].

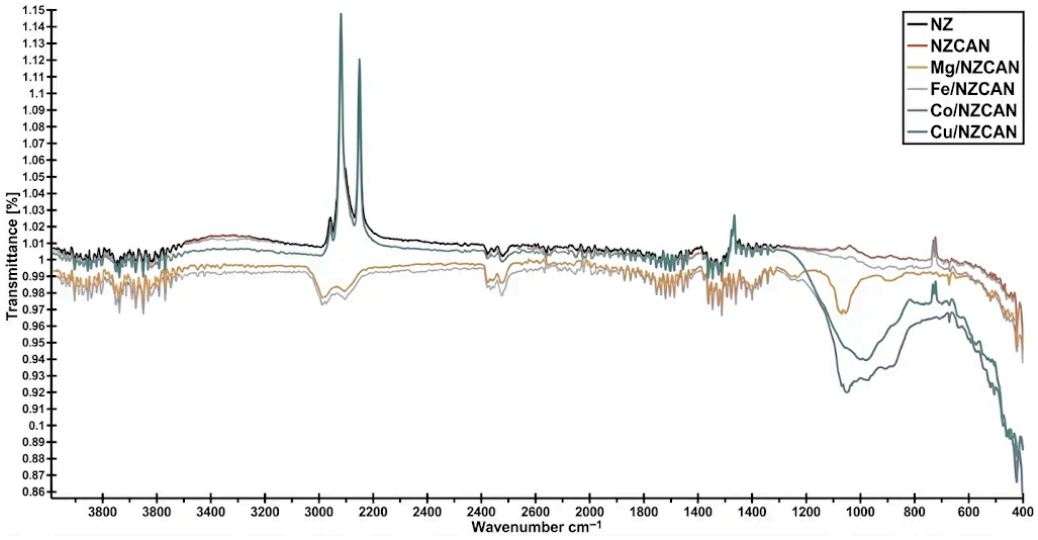

Figure 5. FTIR spectra of NZ, NZCAN, Mg/NZCAN, Cu/NZCAN, Co/NZCAN, and Fe/NZCAN.

The FTIR spectrum of the NZCAN sample displayed the main characteristic bands of the aluminosilicate framework (Figure 5). The asymmetric stretching vibration of Si–O–Si/Si–O–Al bonds was responsible for the appearance of a strong and wide band at 1055, 1066, and 1075 cm^{-1}. The Si–O/Al–O bending vibrations of the framework were identified by a set of medium-intensity, regular bands at 421, 446, 458, 473, 502, 517, and 525 cm^{-1} in the low-wavenumber region. Furthermore, very weak bands were seen at 1457, 2973, and 2988 cm^{-1}, which could be the result of trace amounts of organic molecules' C–H vibrations. The primary framework bands indicate the preservation of the aluminosilicate structure in the NZCAN sample [13].

The FTIR spectrum of the Cu/NZCAN sample showed noticeable changes compared with the support alone (Figure 5). An interaction between the copper species and the aluminosilicate framework is indicated by the major asymmetric stretching vibration of Si–O–Si/Si–O–Al bonds, which appeared as a very strong and broad band at 976 cm^{-1} and shifted to a lower wavenumber relative to NZCAN (1055–1075 cm^{-1}). The H–O–H bending vibration of adsorbed or coordinated water was identified as the cause of the medium-to-low intensity bands seen at 1653, 1684, and 1699 cm^{-1}. The symmetric stretching vibration of Si–O–Si/Si–O–Al bonds was identified as the source of weak to medium bands at 668, 725, and 765 cm^{-1} [20]. The presence of copper oxide species on the surface is suggested by the appearance of a strong and clear band at 569 cm^{-1}, which is indicative of Cu–O bending vibration. Additionally, medium-intensity bands at 418 and 457 cm^{-1} were attributed to aluminosilicate framework vibrations involving Cu–O and Si–O/Al–O bending modes. Overall, the Cu–O band's appearance and the main framework band's shift show that copper was successfully incorporated into the NZCAN support [51].

The Si–O–Si/Si–O–Al framework connections were represented by a strong and broad asymmetric stretching band at 1052, 1068, and 1076 cm^{-1} in the FTIR spectra of the cobalt-loaded clinoptilolite sample (Co/NZCAN) as shown in Figure 5. This band's location did not significantly change in relation to NZCAN, suggesting that the cobalt inclusion did not affect the aluminosilicate framework. Furthermore, medium-intensity bands were detected at 1653, 1684, 1699, and 1717 cm^{-1}, which were attributed to the H–O–H bending vibration of coordinated or adsorbed water. Adsorbed water and surface hydroxyl (–OH) groups were identified as the source of sharp, well-resolved bands at 3750 cm^{-1}. The

symmetric stretching vibrations of Si–O–Si/Si–O–Al connections were identified as weak bands at 853 and 899 cm^{-1}. Additionally, a medium-intensity band at 668 cm^{-1} associated with Co^{3+}–O species suggested the presence of mixed-valence cobalt oxide species on the support, whereas distinct and sharp bands at 517, 527, and 569 cm^{-1} showed the presence of Co^{2+}–O bonds. Lastly, the Si–O/Al–O bending modes of the framework were represented by the bands at 419 and 468 cm^{-1} [20,52].

The asymmetric stretching vibration of Si–O–Si/Si–O–Al framework connections gives the strong and broad band in the 1050–1080 cm^{-1} region of the iron-loaded clinoptilolite sample (Fe/NZCAN) FTIR spectrum as shown in Figure 5. This band's location did not significantly change in relation to NZCAN, suggesting that the aluminosilicate structure remained intact following iron loading. Strong and overlapping bands at 527, 591, 634, and 669 cm^{-1} were identified as Fe–O vibrations that overlapped with the zeolite's framework modes, indicating the existence of iron oxide species on the support. The H–O–H bending vibration of adsorbed or coordinated water was identified as the source of weak bands at 1684, 1699, and 1717 cm^{-1}. The sharp bands at 3735 and 3750 cm^{-1} in the high-wavenumber region were attributed to terminal (isolated) silanol groups (Si–OH) on the external surface, whereas the bands at 3649 and 3675 cm^{-1} were attributed to bridging hydroxyl groups (Si–OH–Al) and/or hydroxyl groups associated with metal species, along with adsorbed water. Additionally, medium-intensity bands at 419, 437, and 454 cm^{-1} matched the framework's Si–O/Al–O bending modes, supporting the zeolite structure's preservation following iron alteration [20,49].

Compared to the NZCAN material, no significant change was observed in the Fourier-transform infrared (FTIR) spectrum of the Mg/NZCAN material (Figure 5). The appearance of a broad, intense band in the 1000–1100 cm^{-1} range was attributed to the asymmetric stretching vibrations of the Si–O–Si/Si–O–Al framework bonds, indicating that the aluminosilicate framework remains intact following the loading of magnesium. Furthermore, bands of weak to medium intensity at wavenumbers 1653, 1684, 1699, and 1717 cm^{-1} were identified as arising from the bending vibrations of adsorbed or coordinately bonded water (H–O–H) molecules. The sharp bands observed at 504 and 526 cm^{-1} were attributed to Mg–O bond vibrations, indicating the presence of magnesium oxide species on the support material. The bands observed at 3735 and 3750 cm^{-1} in the high-wavenumber region have been identified as terminal (isolated) silanol (Si–OH) groups, while the bands at 3649 and 3675 cm^{-1} are attributed to bridging hydroxyl groups (Si–OH–Al) and/or hydroxyl groups associated with metal species, in addition to the presence of adsorbed water. Finally, the bending modes of the Si–O/Al–O bonds within the framework are responsible for the medium-intensity bands at 419, 434, 446, and 473 cm^{-1}, providing further evidence that the zeolite structure remained intact following modification with magnesium [39,45].

Among all the samples, the NZCAN zeolite had the largest surface area (26.32 m^2/g) after being heat-treated at 500 °C and cleaned with nitric acid. Clinoptilolite is characterized by a microchannel structure, which gives it high selectivity for molecules, a trait typical of this type of zeolite [13,33]. The 500 °C temperature expelled water molecules and organic matter trapped within the microchannels, activating the surface and opening blocked pores. It has been shown that clinoptilolite maintains good structural stability up to 700 °C. However, 500 °C is the optimal temperature, as it does not activate zeolite or damage its crystalline framework. Natural ions present in the structural framework at ion-exchange sites, such as Na, K, C, O, and Ca, may have been removed by washing with nitric acid [33]. This was also confirmed by EDS assay, where the proportions of these ions decreased, as shown in Figure 6. Partial removal of alumina also increased the Si/Al ratio, which produced additional secondary porosity and helped to clean the surface of the material from metallic impurities [35].

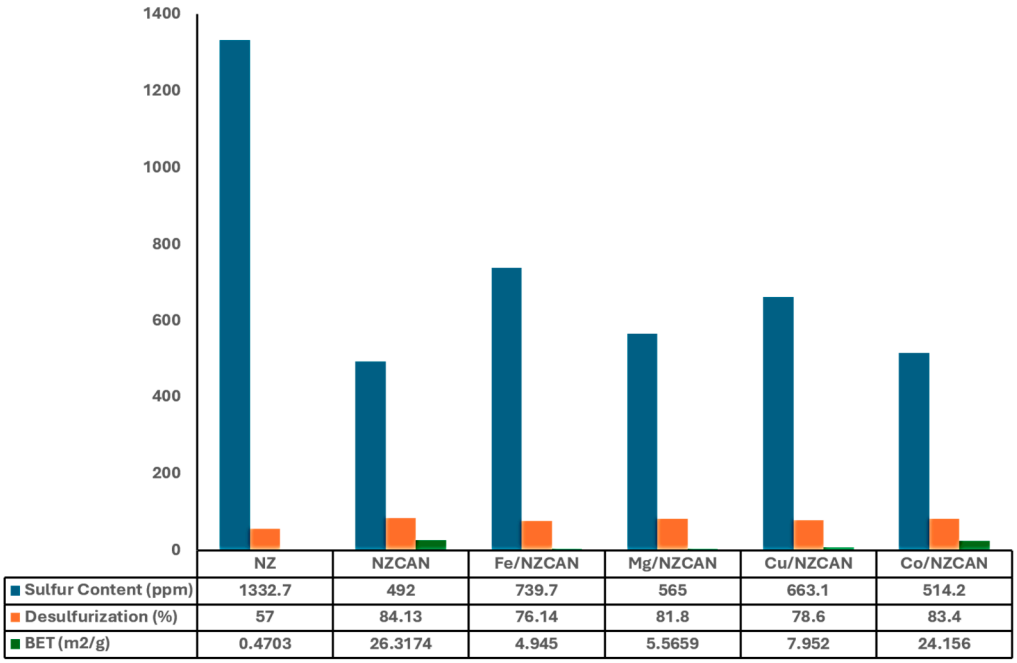

	NZ	NZCAN	Fe/NZCAN	Mg/NZCAN	Cu/NZCAN	Co/NZCAN
Sulfur Content (ppm)	1332.7	492	739.7	565	663.1	514.2
Desulfurization (%)	57	84.13	76.14	81.8	78.6	83.4
BET (m2/g)	0.4703	26.3174	4.945	5.5659	7.952	24.156

Figure 6. Comparison of the residual sulfur content and desulfurization efficiency of clinoptilolite catalysts after 140 min and 35 °C of oxidative desulfurization.

Mg/NZCAN yielded a surface area of 5.5659 m^2/g, which is a significant decrease in surface area, exceeding 79%, compared to NZCAN. Several studies have indicated that high-charge-density Mg^{2+} ions, with their small radius 0.72 Å and high hydration energy, tend to form MgO oxide clusters at the channel inlets when deposited on clinoptilolite, rather than being distributed uniformly within them. This would reduce the pore free diameter and prevent nitrogen atoms used in BET measurement from reaching the zeolite's internal surface. The calcination following the mineral loading process may further promote the agglomeration and expansion of these oxides within the pore structure [39,44].

As for Cu/NZCAN, its surface area was found to be 7.95 m^2/g. This is slightly better than Mg-zeolite but still about 70% lower than NZCAN. Cu^{2+} in clinoptilolite tends to occupy exchange sites via a selective ion-exchange mechanism. However, loading it at a concentration of 0.2 M for 5 h at 70 °C may have caused partial precipitation of some copper oxides, CuO, or hydroxides on the outer surface of the zeolite and at the mouths of its channels. This could explain the reduction in the effective surface area [19]. However, it is noted that copper is less prone to clumping compared to magnesium, which explains the slight difference between their values [20].

For the Co/NZCAN, the results were particularly noteworthy with a surface area of 24.16 m^2/g that was only slightly reduced by 8% compared to NZCAN. This exceptional behavior indicates that the Co^{2+} ions, with a radius of 0.745 Å, performed homogeneous and orderly ion exchange with exchangeable ions at the M2 and M4 sites of the clinoptilolite structure, thus keeping the zeolite channels largely permeable [20]. Previous studies have confirmed that cobalt exhibits exceptional structural compatibility with the clinoptilolite crystal framework, making it the most suitable loading mineral in terms of preserving the material's porous properties [20,53]. This characteristic makes Co-Clinoptilolite structurally particularly attractive for adsorption applications, as it combines the presence of active mineral sites with a large active surface area [47,54].

Finally, the Fe/NZCAN recorded a surface area of 4.94 m^2/g, the lowest of all the samples tested. The chemical composition of Fe^{3+} ions in aqueous solution is responsible for this dramatic drop since they easily produce iron hydroxides $Fe(OH)_3$ and oxyhydroxides

(FeOOH, Fe_2O_3) at a relatively low pH. These gelatinous, colloidal deposits tend to clump together and block the entrances of clinoptilolite channels much more effectively than other divalent metal ions [49]. Furthermore, Fe^{3+} ions may precipitate in greater quantities per unit weight due to their higher charge neutralization requirements compared to Mg^{2+}, Cu^{2+}, and Co^{2+} [20].

The external morphology (extent of surface deposit) of the catalyst has been highlighted by SEM, while the BET analysis indicated the micropores (internal porosity) that are not indicated by the SEM. The visible surface coverage is consistent with the loss of surface area. Co/NZCAN had the lowest deposits and retained 92% of the NZCAN surface area. Aggregated and uneven deposits led to a loss of 70% and 79% when loaded with Cu and Mg, respectively. Loading with Fe led to the greatest loss of 81% attributed to uniform coverage of the surface area and pore entrances by fine iron hydroxide/oxide deposits, consistent with the iron oxide reflection observed by XRD at 52.34°. Across the five analyzed samples, sulfur removal correlated positively with BET; this is regarded as a trend rather than a statistically established relationship.

EDS analysis was performed only for NZ and NZCAN samples; however, metal incorporation was supported by XRD analysis in Figure 4. A reflection at $2\theta = 52.34°$ present in the FE/NZCAN samples is attributed to an iron oxide phase. A strong reflection at 56.68° indicates redistribution of peak intensities in the Mg/NZCAN sample. Furthermore, FTIR analysis further confirmed the presence of Cu at 765 cm^{-1} for Cu/NZCAN, (Co–OH) at 517 cm^{-1} for Co/NZCAN, 437 cm^{-1} (Fe–O) and 634 cm^{-1} (Fe–O–Si) for Fe/NZCAN, and 446–504 cm^{-1} (Mg–O–Si) for Mg/NZCAN. None of the above were present in the FTIR analysis of the NZCAN sample. The results from both the SEM and BET techniques concur that the metal remained present in the samples.

As illustrated in Figure 6, the relationship between ODS of kerosene and metal loading reveals the significance of these results in the context of the selective oxidation of sulfur compounds using a formic acid/hydrogen peroxide system [22]. This process involves two stages: the oxidation of sulfur compounds (thiophene, benzthiophene, and similar compounds) to sulfoxides and sulfones by H_2O_2 in the presence of formic acid, which catalyzes the formation of peroxyformic acid as the oxidizing agent; and the subsequent adsorption of these highly polar oxidized compounds onto the zeolite surface [47]. In this context, Co/NZCAN provides the largest number of active sites for both stages due to its high surface area, while Fe/NZCAN's lower performance was probably caused by two factors: first, compared to the other materials, it had the smallest surface area, which reduced the number of accessible sites for bulky sulfur compounds and their oxidation products. Additionally, it is possible that the iron oxide particles broke down some of the hydrogen peroxide (H_2O_2) without oxidizing the sulfur compounds, which would have decreased the amount of oxidizing agent available for the reaction [4,20,55].

To evaluate the impact of these structural changes on performance, the results of the desulfurization process were examined. Under the measured conditions, acid-treated clinoptilolite (NZCAN) produced the best desulfurization result, reducing the residual sulfur to 492 ppm, which is lower than all metal-loaded samples. At 514.2 ppm, only 22.2 ppm higher than NZCAN, Co/NZCAN was the best metal-loaded material. Additionally, it retained the majority of its surface area (24.16 m^2/g as opposed to NZCAN's 26.32 m^2/g), indicating a well-dispersed metal phase with minimal pore blockage. Large sulfur-containing molecules were able to freely diffuse toward the active sites and transfer mass thanks to this well-preserved porosity structure, which ultimately produced the maximum removal efficiency. The behavior of the other metals was different. Mg/NZCAN, Cu/NZCAN, and Fe/NZCAN left more sulfur in the fuel (565, 663.1, and 739.7 ppm) and had much smaller surface areas (5.66, 7.95, and 4.94 m^2/g, respectively) as shown in Figure 6. Agglomerated

metal species obstructing the micro/mesopores produced by acid activation are consistent with these drops. Fe/NZCAN performed the worst, and its XRD pattern revealed crystalline iron oxide reflections, indicating that excessive iron compound deposition resulted in severe pore blockage, filling the micro/mesoporous network generated by nitric acid activation. Clinoptilolite channels are too narrow for most thiophenic compounds in kerosene and their oxidized products; hence, adsorption is expected to occur mainly on the external surface and at the pore mouth. This leads to making metal deposition at the pore mouths unfavorable for two reasons: they block accessible surface to the sulfur compounds, and the metals that sit inside the microspores remain inaccessible to these compounds [4]. Although Fe/NZCAN showed uniform particle dispersion in the SEM analysis, it showed a lower desulfurization efficiency of 76.14%. Uniform dispersion does not correlate with accessible active sites. That fine Fe particles cover the surface and pore entrances uniformly may explain the lowest surface area [56].

Since all the samples were tested under identical conditions of oxidation and extraction, the difference in removal rates is attributed to the solids even though the H_2O_2/HCOOH system itself is capable of oxidizing sulfur contents. The removal efficiency broadly followed the surface area where the higher achieved removal rate of 84.13% was achieved utilizing NZCAN sample. None of the transition metals improved the removal efficiency suggesting that the role of zeolite is adsorptive and retention of the oxidized sulfur products rather than metal-centered catalytic oxidation. Two detrimental effects explain the lowered metal-loaded sample performance. Firstly, metal loading led to reduced BET and partially blocked the channels as illustrated by SEM images limiting the adsorption of the polar oxidized sulfur species. Secondly, redox activity associated with Fe, Cu, and Co is known to decompose H_2O_2 and reduce the oxidant available for peroxyformic acid formation [57]. To demonstrate the two effects, comparing Mg/NZCAN with Cu/NZCAN will help separate the effects. The non-redox Mg/NZCAN sample achieved a higher removal rate of 81.8% when compared to Cu/NZCAN which achieves a removal rate of 78.6% despite the latter having higher surface area. This suggests that the redox activity of Cu had an additional penalty combined with pore blockage. This is consistent with the lowest removal rate of 76.14% attributed to the highest expected H_2O_2 decomposition. On the other hand, the load of Co neither helped nor hindered the process. Although the actual metal loading was not measured, the main conclusion that none of the metal-loaded samples exceeded the performance of NZCAN still holds regardless of the actual loading. ICP-OES quantification is recommended for future work. The location and oxidation state of the metal species were not determined directly; SEM-EDS mapping, pore size and XPS analysis are planned for future work.

The current method operates at 35 °C and atmospheric pressure without the need for hydrogen, compared to the traditional hydrodesulfurization (HDS) process, which operates at temperatures between 300 °C and 400 °C under high hydrogen pressure and uses a commercial catalyst that costs roughly (15–35) $/kg (a rough estimate subject to market prices and exchange rates). This method's gentle working conditions are its main advantage. Natural clinoptilolite, a plentiful and inexpensive mineral (0.05–0.20) $/kg [58] is the source of NZCAN. On a laboratory scale, the whole cost of its synthesis, which includes chemical activation with 2 M nitric acid (at a ratio of 2 L/kg) and heat treatment at 500 °C for 4 h, is roughly 12–17 $/kg [58], with thermal energy making up the majority of this expense. By using industrial-grade acid and a rotating kiln, this number is anticipated to drop on an industrial scale. However, determining the cost per unit of sulfur removed based on the material's adsorption capacity and the number of reuse cycles is still necessary for an accurate economic comparison. NZCAN was also reported to be the most effective sample of all the 5 tested samples. The HNO_3 treatment of the NZCAN sample removes exchangeable cations and hence may limit leaching during reaction. In contrast, the metal-

loaded samples, particularly Co/NZCAN, carry a higher potential risk of metal leaching into the fuel or aqueous phase, which is a further practical reason to prefer the unloaded material. The regenerated NZCAN sample retained an 83.9% removal rate, indicating reusability. Metal leaching, structural stability after repeated use and solvent recovery were not assessed in the present study and will be examined in future work, including ICP analysis of the treated fuel and post-reaction XRD.

The FTIR spectrum for regenerated NZCAN is shown in Figure 7a, where the surface is rich in OH groups as indicated by the spectrum's many peaks in the OH region at 3853, 3735, 3675, 3649, 3629, and 3567 cm^{-1} [59]. This could be explained by the adsorption of moisture after activation or by the effects of the oxidizing agent (peroxide) and formic acid. H-O-H bending or carbonyl groups from the oxidation of organic materials are responsible for the peaks at 1699, 1684, and 1653 cm^{-1} [12]. At 2916 and 2848 cm^{-1} (CH_2 stretching), 1463 cm^{-1} (bending), and 718 cm^{-1} (rocking), peaks belonging to aliphatic C-H bonds appear inverted (with a transmittance larger than 100%). This shows that the activation process successfully eliminated the adsorbed kerosene because the activated sample has fewer hydrocarbons than the reference material [12]. The crystalline structure appears to be intact after the adsorption–activation cycle by the appearance of a band linked to Si-O and Al-O bonds at 1057 cm^{-1}, along with peaks at 772 and 669 cm^{-1}, all indicative of zeolitic framework vibrations [12]. The crystalline structure of the sample remains intact; neither the adsorption–activation cycle nor the thermal and acid treatments appear to have caused any structural collapse. An increase in hydroxyl (OH) groups, along with the appearance of peaks in the 1653–1699 cm^{-1} range associated with carbonyl groups or water (potentially originating from formic acid, peroxides, or the presence and adsorption of moisture) indicates oxidative surface activity in the regenerated sample. Furthermore, the absence of aliphatic peaks suggests that the activation process, conducted at 400 °C in a nitrogen atmosphere, effectively removes carbon–hydrogen (C–H) bonds from the sample. The sample shows no discernible hydrocarbon adsorption, which is in line with how well the activation procedure eliminates kerosene [60].

The regenerated sample's XRD pattern in Figure 7b shows that it still has the distinctive peaks of the original material, including large peaks at 27.6°, 29.9–30.9°, 35.5°, 56.8°, and 62.5°, as well as reflections characteristic of clinoptilolite in the 22–24° range; this indicates that the crystal structure was largely preserved after regeneration at a temperature of 400 °C. There is no discernible peak broadening or emergence of additional phases (the strongest peak's full width at half maximum, or FWHM, is 0.154° as opposed to 0.116° for the raw material). Additionally, the pattern is consistent with the sample spent after sulfur adsorption and oxidation [41]. The FTIR spectrum, which shows an Al–O/Si–O band at 1057 cm^{-1}, supports this. When combined, these findings show that after the adsorption cycle and subsequent thermal activation under nitrogen, the crystalline structure does not collapse; as a result, the sample is a good candidate for reactivation with nitric acid for use in a further adsorption cycle.

The morphology of the regenerated sample is visible in an SEM picture at 10,000× magnification (scale bar: 5 μm), as shown in Figure 7c. In keeping with the well-known lamellar structure of clinoptilolite, the granule is made up of overlapping plates and sheets with straight edges and comparatively acute angles. A possible indicator of secondary porosity (meso-/macroporosity) in the sample is a recessed area (cavity) near the image's center that has a fine, porous, sponge-like texture made up of a network of tiny voids and short, needle-like or rod-shaped structures connected to a narrow fissure. The bottom left corner likewise exhibits a comparable fine-grained surface texture. The lateral surfaces are comparatively smooth and stepped, and they are dotted with tiny particles that range in size from a few micrometers to sub-micrometers. These particles are probably surface

deposits, related mineral phases, or grinding dust. There are no indications of melting, vitrification, fused agglomerates, or significant fragmentation in the picture. Additionally, the XRD results, which show no new phases or structural collapse, are supported by the lamellar framework's lack of severe erosion. This suggests that the adsorption, oxidation, and heat activation processes did not result in any notable morphological degradation.

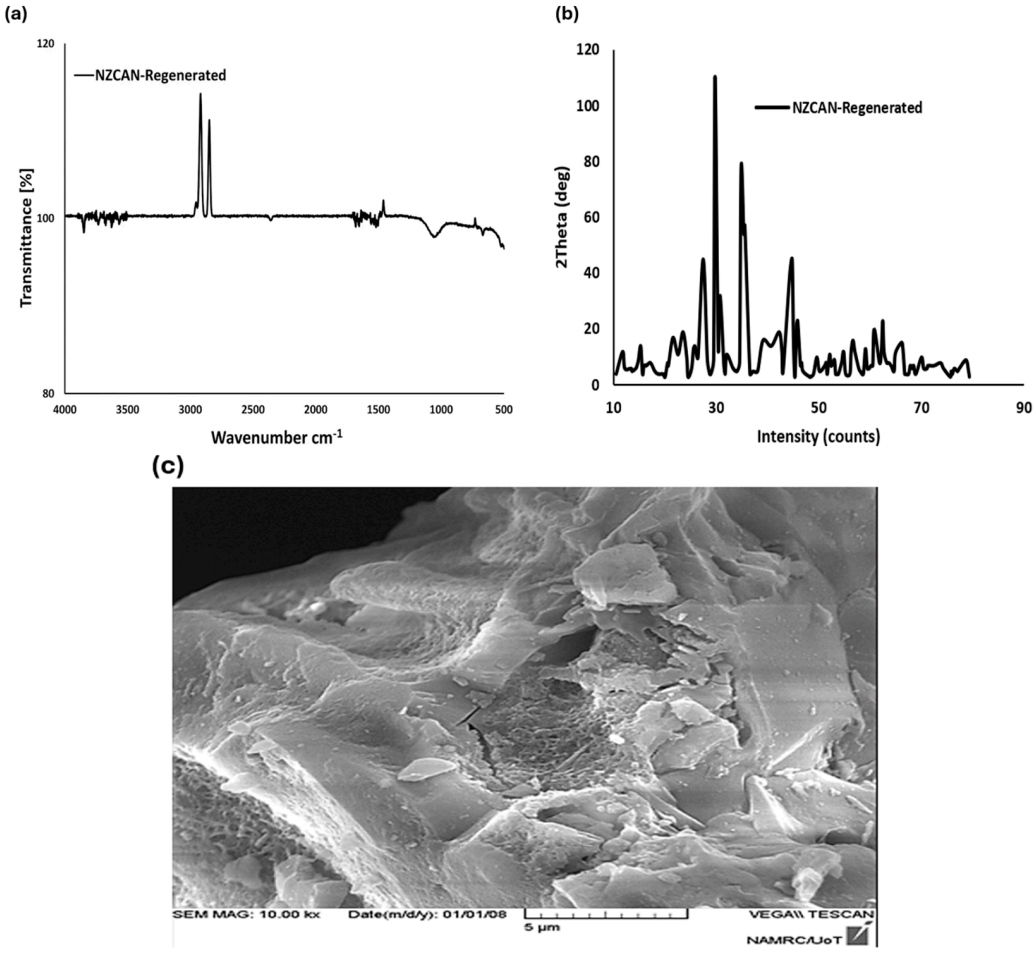

Figure 7. (**a**) FTIR spectra, (**b**) XRD, and (**c**) SEM of NZCAN regenerated sample.

It was suggested that multi-cycle testing be done as a next step, as in the current study just one regeneration cycle was carried out. The regenerated NZCAN material preserved almost 99.8% of its initial efficiency after a single regeneration cycle, achieving a desulfurization efficiency of 83.9% (with 499.1 ppm of sulfur remaining) as opposed to 84.1% for the fresh sample.

4. Conclusions

Using actual kerosene feedstock from the Al-Shanafiyah refinery, the removal efficiency increased from 57% (NZ) to 84.13% (NZCAN), indicating that heat and acidic activation were the primary factors responsible for the higher desulfurization performance of natural clinoptilolite. The removal efficiency was not further enhanced by loading the activated zeolite with transition metals. Among the metal-loaded samples, removal efficiency followed the order Co > Mg > Cu > Fe (83.4%, 81.8%, 78.6%, and 76.14%, respectively), all lower than NZCAN. The majority of the loaded samples had a reduction in surface area and partial pore blockage due to the deposited metal particles, which are consistent with the BET and SEM data. Among the metals studied, cobalt loading produced the greatest results

and maintained the largest surface area (24.16 m^2/g), making it the best choice if loading is necessary for additional applications. These findings suggest that heat and acidic activation alone, without any metal loading, are sufficient to achieve a high desulfurization efficiency, which simplifies and lowers the cost of the process. The spent NZCAN sample was cleaned and re-activated by calcination at 400 °C for 120 min as part of an initial reusability test. The material can be reused without experiencing a significant decline in performance, as evidenced by the regenerated sample's removal efficiency of 83.9%, which was comparable to the fresh sample. A more comprehensive study involving many regeneration cycles is planned as a separate project.

Author Contributions: Conceptualization, D.J.H. and H.S.; methodology, M.A.M.; validation, H.S., D.J.H. and H.S.; formal analysis, C.T.T.; investigation, D.J.H.; resources, M.A.M.; data curation, D.J.H.; writing—original draft preparation, D.J.H.; writing—review and editing, H.S.; visualization, M.R.O.; supervision, M.R.O., C.T.T. and M.A.M.; project administration, M.R.O., C.T.T. and M.A.M. All authors have read and agreed to the published version of the manuscript.

Funding: This research received no external funding.

Data Availability Statement: Data will be made available upon reasonable request.

Acknowledgments: The authors gratefully acknowledge the support from the Universiti Sains Malaysia through GRA-Assist.

Conflicts of Interest: The authors declare no conflicts of interest.

References

1. Kanjal, M.I.; Yasmin, I.; Afzal, M.W.; Sabir, S.; Kavitha, P.; Pang, J.-Y.; Dang, D.-B.; Zhu, W.-S.; Bai, Y. Innovative approaches to navigate the challenges in photocatalytic oxidation desulfurization of fuel: A systematic review. *Green Chem. Eng.* **2027**, *8*, 7–26. [CrossRef]
2. Siddiqui, S.U.; Ahmed, K. METHODS FOR DESULFURIZATION OF CRUDE OIL-A REVIEW. *Sci. Int.* **2016**, *28*, 1169–1173.
3. Hussein, H.Q.; Ali, S.M.; Altabbakh, B.A.A.; Hussein, S.J.; Ali, Y.M.; Ibrahim, S.K.; Yousif, S.A. Hydrodesulfurization and Hydrodearomatization of Kerosene over high metal loading Ni w/γ-Al_2O_3 Catalyst. *J. Pet. Res. Stud.* **2021**, *8*, 28–46. [CrossRef]
4. Mahmoudi, R.; Falamaki, C. A Systematic Study on the Effect of Desilication of Clinoptilolite Zeolite on its Deep-Desulfurization Characteristics. *Nanochem Res.* **2016**, *1*, 205–213. [CrossRef]
5. Jarullah, A.; Mohammed, H.J. Experimental Design of Oxidative Desulfurization of Kerosene Through Response Surface Methodology (RSM). *Tikrit J. Eng. Sci.* **2023**, *30*, 130–141. [CrossRef]
6. Kanjal, M.I.; Muneer, M.; Saeed, M.; Chu, W.; Alwadai, N.; Iqbal, M.; Abdelhaleem, A. Oxone activated TiO_2 in presence of UV-LED light for the degradation of moxifloxacin: A mechanistic study. *Arab. J. Chem.* **2022**, *15*, 104061. [CrossRef]
7. Favvas, E.P.; Tsanaktsidis, C.G.; Sapalidis, A.A.; Tzilantonis, G.T.; Papageorgiou, S.K.; Mitropoulos, A.C. Clinoptilolite, a natural zeolite material: Structural characterization and performance evaluation on its dehydration properties of hydrocarbon-based fuels. *Microporous Mesoporous Mater.* **2016**, *225*, 385–391. [CrossRef]
8. Ammar, S.H.; Kareem, Y.S.; Mohammed, M.S. Catalytic-oxidative/adsorptive denitrogenation of model hydrocarbon fuels under ultrasonic field using magnetic reduced graphene oxide-based phosphomolybdic acid (PMo-Fe_3O_4/rGO). *Ultrason. Sonochemistry* **2020**, *64*, 105050. [CrossRef] [PubMed]
9. Humadi, J.I.; Shihab, M.A.; Hasan, A.A.; Mohammed, A.M. Experimental and ANN modeling of kerosene fuel desulfurization using a manganese oxide-tin oxide catalyst. *Chem. Eng. Res. Des.* **2024**, *211*, 160–167. [CrossRef]
10. Siora, I.; Andriyko, L.; Gerashchenko, I.; Borysenko, M.; Pakhlov, E.; Oranska, O.; Lytvynenko, Y.; Tsyba, M.; Odynchenko, R.; Goncharuk, O. Comparative study of the structural characteristics and adsorption capacity of natural and synthetic zeolites. *Microporous Mesoporous Mater.* **2025**, *397*, 113778. [CrossRef]
11. Armbruster, T. Clinoptilotite-heulandite: Applications and basic research. *Stud. Surf. Sci. Catal.* **2001**, *135*, 13–27. [CrossRef]
12. Mozgawa, W.; Król, M. FT-IR studies of zeolites from different structural groups. *CHEMIK* **2011**, *65*, 667–674.
13. Yossifova, M.; Dimitrova, D.; Ivanova, R.; Tzvetanova, Y.; Lyutov, G.; Sergeeva, I. Mineral and Chemical Composition of Selected Clinoptilolite Tuffs and Migration of Elements in Acidic Aqueous Media. *Proc. Bulg. Acad. Sci.* **2021**, *74*, 1012–1023. [CrossRef]
14. Liu, Y.; Zhao, S.; Qiu, X.; Meng, Y.; Wang, H.; Zhou, S.; Qiao, Q.; Yan, C. Clinoptilolite based zeolite-geopolymer hybrid foams: Potential application as low-cost sorbents for heavy metals. *J. Environ. Manag.* **2023**, *330*, 117167. [CrossRef] [PubMed]

15. Yoosuk, B.; Silajan, A.; Prasassarakich, P. Deep adsorptive desulfurization over ion-exchanged zeolites: Individual and simultaneous effect of aromatic and nitrogen compounds. *J. Clean. Prod.* **2020**, *248*, 119291. [CrossRef]
16. Biblioteca, I.; Sambucci, M.; Valente, M. Zeolite-Clinoptilolite conditioning for improved heavy metals ions removal: A preliminary assessment. *Ceram. Int.* **2023**, *49*, 39649–39656. [CrossRef]
17. Rezvani, M.A.; Ghasemi, K.; Ardeshiri, H.H.; Aghmasheh, M. Deep oxidative desulfurization of gas oil by iron(III)-substituted polyoxometalate immobilized on nickel(II) oxide, ((n-C4H9)4N)4H[PW11FeO39]@NiO, as an efficient nanocatalyst. *Sci. Rep.* **2023**, *13*, 15233. [CrossRef] [PubMed]
18. Akopyan, A.V.; Eseva, E.A.; Tsaplin, D.E.; Latypova, S.S.; Makeeva, D.A.; Anisimov, A.V.; Maximov, A.L.; Karakhanov, E.A. Deep aerobic desulfurization of fuels over iron–containing zeolite-based catalysts. *Chem. Eng. J. Adv.* **2022**, *12*, 100385. [CrossRef]
19. Mamaghani, A.H.; Fatemi, S.; Asgari, M. Investigation of Influential Parameters in Deep Oxidative Desulfurization of Dibenzothiophene with Hydrogen Peroxide and Formic Acid. *Int. J. Chem. Eng.* **2013**, *2013*, 951045. [CrossRef]
20. Sobuś, N.; Król, M.; Piotrowski, M.; Michorczyk, B.; Czekaj, I.; Kornaus, K.; Trenczek-Zając, A.; Komarek, S. Conversion of dihydroxyacetone to carboxylic acids on pretreated clinoptilolite modified with iron, copper, and cobalt. *Catal. Commun.* **2022**, *171*, 106509. [CrossRef]
21. Seyedi, M.S.; Bahmaei, M.; Farshi, A. Oxidative desulfurization of kerosene in the presence of iron chloride ionic liquid catalyst and ultrasound waves. *Orient. J. Chem.* **2015**, *31*, 2409–2413. [CrossRef]
22. Salavati-Niasari, M. Zeolite-encapsulation copper(II) complexes with 14-membered hexaaza macrocycles: Synthesis, characterization and catalytic activity. *J. Mol. Catal. A Chem.* **2004**, *217*, 87–92. [CrossRef]
23. Tomar, S.S.; Verma, N.; Nigam, K.D.P. Adsorptive desulfurization of thiophene using Cu-CNF slurry in a coiled flow inverter with recycling. *Chem. Eng. Sci.* **2023**, *281*, 119172. [CrossRef]
24. Salavati-Niasari, M.; Shakouri-Arani, M.; Davar, F. Flexible ligand synthesis, characterization and catalytic oxidation of cyclohexane with host (nanocavity of zeolite-Y)/guest (Mn (II), Co (II), Ni (II) and Cu (II) complexes of tetrahydro-salophen) nanocomposite materials. *Microporous Mesoporous Mater.* **2008**, *116*, 77. [CrossRef]
25. Subhan, F.; Aslam, S.; Yan, Z.; Yaseen, M. Highly dispersive Cu species constructed in mesoporous silica derived from ZSM-5 for batch and continuous adsorptive desulfurization of thiophene. *Fuel Process. Technol.* **2022**, *235*, 107351. [CrossRef]
26. Kumagai, S.; Shimizu, Y.; Toida, Y.; Enda, Y. Removal of Dibenzothiophenes in Kerosene by Adsorption on Rice Husk Activated Carbon. *Fuel* **2009**, *88*, 1975. [CrossRef]
27. Nyankson, E.; Efavi, J.K.; Yaya, A.; Manu, G.; Asare, K.; Daafuor, J.; Abrokwah, R.Y. Synthesis and characterisation of zeolite-A and Zn-exchanged zeolite-A based on natural aluminosilicates and their potential applications. *Cogent Eng.* **2018**, *5*, 1440480. [CrossRef]
28. Jääskeläinen, H. Fuel Property Testing: Sulfur. DieselNet Technology Guide. What is Diesel Fuel. Available online: https://dieselnet.com/tech/fuel_diesel_sulfur.php#d7039 (accessed on 16 October 2026).
29. Armandsefat, F.; Hamzehzadeh, S.; Azizi, N. Efficient and promising oxidative desulfurization of fuel using Fenton like deep eutectic solvent. *Sci. Rep.* **2024**, *14*, 12614. [CrossRef] [PubMed]
30. Jiang, W.; Zhu, W.; Li, H.; Chao, Y.; Xun, S.; Chang, Y.; Liu, H.; Zhao, Z. Mechanism and optimization for oxidative desulfurization of fuels catalyzed by Fenton-like catalysts in hydrophobic ionic liquid. *J. Mol. Catal. A Chem.* **2014**, *382*, 8–14. [CrossRef]
31. Centi, G.; Perathoner, S.; Torre, T.; Verduna, M.G. Catalytic wet oxidation with H_2O_2 of carboxylic acids on homogeneous and heterogeneous Fenton-type catalysts. *Catal. Today* **2000**, *55*, 61–66. [CrossRef]
32. Li, L.Y.; Tazaki, K.; Lai, R.; Shiraki, K.; Asada, R.; Watanabe, H.; Chen, M. Treatment of acid rock drainage by clinoptilolite—Adsorptivity and structural stability for different pH environments. *Appl. Clay Sci.* **2008**, *39*, 1–9. [CrossRef]
33. Czekaj, I.; Sobuś, N. Odors Adsorption in Zeolites Including Natural Clinoptilolite: Theoretical and Experimental Studies. *Materials* **2024**, *17*, 3088. [CrossRef] [PubMed]
34. Alberti, A. The Crystal Structure of Two Clinoptilolites. *Tschermaks Mineral. Und Petrogr. Mitteilungen* **1975**, *22*, 25–37. [CrossRef]
35. Tanirbergenova, S.; Tugelbayeva, D.; Zhylybayeva, N.; Aitugan, A.; Tazhu, K.; Moldazhanova, G.; Mansurov, Z. Effect of Acid Treatment on the Structure of Natural Zeolite from the Shankhanai Deposit. *Processes* **2025**, *13*, 2896. [CrossRef]
36. Abecia, V.M.; Salah, S.; Vasile, M.; Laenen, B.; Regenspurg, S.; Cappuyns, V. Effect of acetate and chloride on Pb sorption onto clinoptilolite at geothermal conditions. *Appl. Geochem.* **2025**, *192*, 106533. [CrossRef]
37. Król, M.; Dechnik, J.; Szymczak, P.; Handke, B.; Szumera, M.; Stoch, P. Thermal Behavior of Clinoptilolite. *Crystals* **2024**, *14*, 646. [CrossRef]
38. Garcia-Basabe, Y.; Rodriguez-Iznaga, I.; de Menorval, L.-C.; Llewellyn, P.; Maurin, G.; Lewis, D.W.; Binions, R.; Autie, M.; Ruiz-Salvador, A.R. Step-wise dealumination of natural clinoptilolite: Structural and physicochemical characterization. *Microporous Mesoporous Mater.* **2010**, *135*, 187–196. [CrossRef]
39. Erdoğan, B.; Ergürhan, O. Natural and pretreated Gördes clinoptilolites for ammonia removal: Effect of exchangeable cations (Na^+, K^+, Ca^{2+} and Mg^{2+}). *Clay Miner.* **2024**, *59*, 39–49. [CrossRef]

40. Kareem, J.H. Oxidative Desulfurization of Diesel Fuel Using Three Kinds of Carboxylic Acids Supported by Iron(III) Chloride. *Polytech. J.* **2021**, *11*, 104–111. [CrossRef]
41. Cerri, G.; Farina, M.; Brundu, A.; Daković, A.; Giunchedi, P.; Gavini, E.; Rassu, G. Natural zeolites for pharmaceutical formulations: Preparation and evaluation of a clinoptilolite-based material. *Microporous Mesoporous Mater.* **2016**, *223*, 58–67. [CrossRef]
42. Grifasi, N.; Ziantoni, B.; Fino, D.; Piumetti, M. Fundamental properties and sustainable applications of the natural zeolite clinoptilolite. *Environ. Sci. Pollut. Res.* **2025**, *32*, 27805–27840. [CrossRef] [PubMed]
43. Kukobat, R.; Škrbić, R.; Massiani, P.; Baghdad, K.; Launay, F.; Sarno, M.; Cirillo, C.; Senatore, A.; Salčin, E.; Atlagić, S.G. Thermal and structural stability of microporous natural clinoptilolite zeolite. *Microporous Mesoporous Mater.* **2022**, *341*, 112101. [CrossRef]
44. Biessikirski, A.; Kaczmarczyk, G.P.; Kolano, M.; Kaznowska-Opala, K.; Ruggiero-Mikołajczyk, M.; Gurgul, J.; Kuterasiński, Ł. Impact of Treatment Methods on the Surface Properties of the Mg-Containing Zeolite Y. *Materials* **2025**, *18*, 1033. [CrossRef] [PubMed]
45. Ünaldı, T.; Orhun, Ö.; Kadir, S. Physicochemical Characterization of Natural and Na^+, K^+, Ca^{2+}, and Mg^{2+} -modified Clinoptilolite from Gördes (Manisa, Turkey). *Adsorpt. Sci. Technol.* **2009**, *27*, 615–631. [CrossRef]
46. Samadi-Maybodi, A.; Trojeni, M.M.; Shafiei, H. Modification of clinoptilolite as a natural zeolite by copper oxide nanoparticles for efficient desulfurization of kerosene. *J. Sulfur Chem.* **2024**, *45*, 1067–1081. [CrossRef]
47. Yu, J.; Zhu, Z.; Ding, Q.; Zhang, Y.; Wu, X.; Sun, L.; Du, J. Oxidative desulfurization of dibenzothiophene with molecular oxygen using cobalt and copper salen complexes encapsulated in NaY zeolite. *Catal. Today* **2020**, *339*, 105–112. [CrossRef]
48. Saleh, T.A.; Al-Hammadi, S.A.; Tanimu, A.; Alhooshani, K. Ultra-Deep Adsorptive Desulfurization of Fuels on Cobalt and Molybdenum Nanoparticles Loaded on Activated Carbon Derived from Waste Rubber. *J. Colloid Interface Sci.* **2018**, *513*, 779–787. [CrossRef] [PubMed]
49. Sobuś, N.; Król, M.; Kouadio, K.S.; Dhainaut, J. Sonochemical modification of clinoptilolite zeolite with iron species: Application to the remediation of methylene blue under photo-Fenton conditions. *Particuology* **2026**, *111*, 58–69. [CrossRef]
50. Baran, R.; Millot, Y.; Onfroy, T.; Krafft, J.M.; Dzwigaj, S. Influence of the nitric acid treatment on Al removal, framework composition and acidity of BEA zeolite investigated by XRD, FTIR and NMR. *Microporous Mesoporous Mater.* **2012**, *163*, 122–130. [CrossRef]
51. Kocasoy, G.; Şahin, V. Heavy metal removal from industrial wastewater by clinoptilolite. *J. Environ. Sci. Health Part A* **2007**, *42*, 2139–2146. [CrossRef] [PubMed]
52. Xu, L.; Huang, H.; Xu, L.; Zhu, D.; Zhang, B.; He, J.; Li, H.; Jiang, W. Encapsulation of cobalt molybdate on modified hierarchical porous TS-1 zeolite catalyst for efficient oxidative desulfurization of fuel. *Sep. Purif. Technol.* **2025**, *354*, 129385. [CrossRef]
53. Bin Lim, J.; Shin, J.; Ahn, N.H.; Heo, I.; Hong, S.B. Selective catalytic reduction of NO with CH_4 over cobalt-exchanged cage-based, small-pore zeolites with different framework structures. *Appl. Catal. B* **2020**, *267*, 118710. [CrossRef]
54. Zhao, H.W.; Li, L.-X.; Zuo, H.-Y.; Qu, D.; Zhang, H.; Tao, L.; Sun, C.-G.; Ju, D.-Y.; An, B.-G. Large-scale synthesis of 3D ordered microporous carbon at low temperature using cobalt ions exchanged zeolite Y as a template. *Xinxing Tan Cailiao/New Carbon Mater.* **2023**, *38*, 861–874. [CrossRef]
55. Te, M.; Fairbridge, C.; Ring, Z. Oxidation reactivities of dibenzothiophenes in polyoxometalate/H_2O_2 and formic acid/H_2O_2 systems. *Appl. Catal. A Gen.* **2001**, *219*, 267–280. [CrossRef]
56. Ding, W.; Zhu, W.; Xiong, J.; Yang, L.; Wei, A.; Zhang, M.; Li, H. Novel heterogeneous iron-based redox ionic liquid supported on SBA-15 for deep oxidative desulfurization of fuels. *Chem. Eng. J.* **2015**, *266*, 213–221. [CrossRef]
57. Lee, K.X.; Valla, J.A. Adsorptive desulfurization of liquid hydrocarbons using zeolite-based sorbents: A comprehensive review. *React. Chem. Eng.* **2019**, *4*, 1357–1386. [CrossRef]
58. Made-in-China. Natural Zeolite. Available online: https://tianhuibao.en.made-in-china.com/product/lgtYHWTxRacM/China-Natural-Clinoptilolite-Zeolite-Powder-for-Water-Purification-Aquaculture-Soil-Amendment-and-Environmental-Treatment.html?header_search_page=lv&pv_id=1k551j3jc0f0&faw_id=1k551j561f9&bv_id=1k551s2pc3b9&pbv_id=1k551j3ooa4cr (accessed on 16 October 2026).
59. Byrappa, K.; Yoshimura, M. *Handbook of Hydrothermal Technology: A Technology for Crystal Growth and Materials Processing*; Noyes Publications: Park Ridge, NJ, USA; William Andrew Pub.: Norwich, NY, USA, 2001.
60. Zaid, S.A.; AbdulRazak, A.A.; Abid, M. A Review of Nano-catalyst Applications in Kerosene Desulfurization Techniques. *J. Appl. Sci. Nanotechnol.* **2022**, *2*, 86–102. [CrossRef]

Disclaimer/Publisher's Note: The statements, opinions and data contained in all publications are solely those of the individual author(s) and contributor(s) and not of MDPI and/or the editor(s). MDPI and/or the editor(s) disclaim responsibility for any injury to people or property resulting from any ideas, methods, instructions or products referred to in the content.